ZSM-5/Silicalite-1 core-shell beads as CO_2 adsorbents with increased hydrophobicity

Boer, D. G.; Asgar Pour, Z.; Poli, S.; Langerak, J.; Bakker, B.; Pescarmona, P. P.

Published in:
Materials Today Chemistry

DOI:
10.1016/j.mtchem.2023.101621

Publication date:
2023

Materials Today Chemistry 32 (2023) 101621

Contents lists available at ScienceDirect

Materials Today Chemistry

journal homepage: www.journals.elsevier.com/materials-today-chemistry/

ZSM-5/Silicalite-1 core-shell beads as CO_2 adsorbents with increased hydrophobicity

D.G. Boer [a, b], Z. Asgar Pour [a], S. Poli [a], J. Langerak [b], B. Bakker [b], P.P. Pescarmona [a, *]

[a] Chemical Engineering Group, Engineering and Technology Institute Groningen (ENTEG), Faculty of Science and Engineering, University of Groningen, Nijenborgh 4, 9747 AG, Groningen, the Netherlands
[b] DMT Environmental Technology, Yndustrywei 3, 8501 SN, Joure, the Netherlands

ARTICLE INFO

Article history:
Received 29 March 2023
Received in revised form
8 June 2023
Accepted 10 June 2023
Available online 11 July 2023

Keywords:
CO_2 adsorption
Hydrophobic zeolite
Biogas upgrading
Core-shell zeolite

ABSTRACT

Zeolites are commonly used for selective CO_2 adsorption from biogas and flue gas. One of the biggest challenges for zeolites in this application is the presence of water vapour in the raw gas streams. While zeolites with low Si/Al ratio typically display high CO_2 adsorption, they are hydrophilic and H_2O competes for adsorption on the active sites. On the other hand, zeolites with high Si/Al ratio are hydrophobic, but display lower CO_2 adsorption capacities. In order to overcome this limitation and to combine the high CO_2 adsorption capacity of low Si/Al zeolites and the hydrophobicity of high Si/Al zeolites into a single material, we designed and synthesized novel core-shell zeolitic beads comprising a ZSM-5 core and a Silicalite-1 shell. Two different strategies were employed to synthesize these macroscopic core-shell beads. In both approaches, the initial step was the synthesis of binderless ZSM-5 beads with hierarchical porosity using resin beads as hard template. In the first strategy, a shell of Silicalite-1 was synthesized on the external surface of the calcined ZSM-5 beads, yielding Sil-ZSM-A core-shell beads (0.84 ± 0.12 mm). In the second strategy, the Silicalite-1 shell was synthesized without first removing the polymeric template from the ZSM-5 beads, resulting in core-shell composite beads that after calcination yielded Sil-ZSM-B core-shell beads (0.73 ± 0.14 mm). Characterization by SEM, XRD, XRF, ICP-AES and N_2 physisorption indicated that both Sil-ZSM-A and Sil-ZSM-B beads displayed the desired zeolitic core-shell structure with hierarchical porosity. Both core-shell beads showed the anticipated increase in hydrophobicity. The most promising results were obtained with Sil-ZSM-A beads, which displayed a 40% decrease in H_2O adsorption capacity at 20% relative humidity (RH) and a 28% decrease at max RH compared to the parent ZSM-5 beads. At the same time, their CO_2 adsorption capacity (1.94 mmol/g at 1 bar) decreased only slightly compared to the parent ZSM-5 beads (2.13 mmol/g at 1 bar). These results indicate that these core-shell beads present the desired combination of the high CO_2 adsorption capacity of the ZSM-5 core with the hydrophobicity of the Silicalite-1 shell. This is a promising feature for application in the adsorption of CO_2 from water-containing streams.

1. Introduction

Carbon dioxide is the most abundant anthropogenic greenhouse gas in the atmosphere and, therefore, has been identified as a major contributor to global warming [1,2]. Carbon Capture Storage and Utilization (CCSU) is considered a viable option to mitigate CO_2 emissions [3,4]. Using this strategy, CO_2 is captured from large point sources, such as power plants, to either achieve long-term storage of CO_2 in the ground (CCS) or, preferably, to employ the CO_2 directly (e.g. as a solvent under supercritical conditions) or as a feedstock for the production of chemicals and synthetic fuels [5–8]. Amongst the most commonly used techniques for CO_2 separation - i.e. absorption in a liquid phase, membrane separation and adsorption on solids - adsorption is considered an attractive technology because it does not generate liquid waste and is a straightforward process [9,10]. Zeolites are an attractive class of materials for CO_2 adsorption due to their high stability, low cost and the possibility to tune their physicochemical properties. For example, by varying the Si/Al ratio, the hydrophobicity of zeolites can be tuned [11]. Besides the removal of CO_2 from flue gas and other CO_2-rich emissions, CO_2 adsorption is also important for the upgrading of biogas, which

* Corresponding author.
E-mail address: p.p.pescarmona@rug.nl (P.P. Pescarmona).

https://doi.org/10.1016/j.mtchem.2023.101621

consists of approximately 40 vol% CO_2 and 60 vol% CH_4. Upgrading of biogas yields bio-methane which is a direct replacement for natural gas. Furthermore, utilization of methane from biogas prevents emission of the greenhouse gas to the atmosphere from e.g. agricultural waste or landfills.

Besides CO_2, biogas and flue gas also contain water vapour in variable amounts (up to 10% for biogas and 20% for flue gas), depending on the specific process conditions [12–14]. Commonly, zeolites with low Si/Al ratio are used for CO_2 adsorption, as the countercations that balance the presence of Al in the zeolite framework are highly active sites for CO_2 adsorption, thus leading to high CO_2 adsorption capacities. However, these zeolites are hydrophilic, and H_2O competes for the active sites, having a stronger interaction with the zeolite compared to CO_2 [15,16]. Therefore, in industrial applications, the bio- or flue gas streams generally require a drying pretreatment [15,17]. This additional step is energy-demanding and, therefore, drives up the cost of the whole separation process. All-silica zeolites are hydrophobic, but their CO_2 adsorption capacity is significantly lower than that of their low Si/Al analogues [18]. A strategy that can allow combining the assets of both types of zeolites consists in coating a low Si/Al zeolite with an all-silica zeolite shell. In such core-shell material, the zeolite with low Si/Al ratio provides high CO_2 adsorption capacity and the all-silica zeolite shell provides the desired hydrophobicity.

In an industrial CO_2 adsorption process, the adsorbent must be macroscopically shaped in order to decrease the pressure drop over the column. For this purpose, zeolites are commonly compressed into the desired shape (e.g. pellets or beads) using an inert binder material (about 20 wt%). The compression and the binder impart mechanical strength to the beads, but this generally leads to a decrease in surface area and in accessibility to the micropores of the zeolitic adsorbent. Furthermore, the binder is typically a poor CO_2 adsorbent, thus leading to a decrease of the CO_2 adsorption capacity per gram of shaped material. An interesting alternative method is the synthesis of binderless zeolitic beads using a hard-templating method [19–21]. The hard template, an anion-exchange resin, shapes the zeolite into a bead format, and upon removal of the template, a network of meso- and macropores is generated which provides access to the micropores of the zeolite. Tosheva et al. first reported the synthesis of Silicalite-1, ZSM-5 and zeolite Beta beads using this hard-templating method [22–24]. Several other zeolites and zeotypes have since been synthesized using this method, such as titanosilicates [25,26], zeolite Beta, ZSM-5 and Faujasite Y as heterogeneous catalysts [27,28]. More recently, we reported the synthesis and application of LTA, Faujasite and SAPO-34 beads as selective CO_2 adsorbents [19–21].

In this work, we combined the assets of the bead morphology with those of a core-shell structure in which the core consists of a zeolite with high CO_2 adsorption capacity and the shell is a zeolite with high Si/Al ratio to provide the desired hydrophobicity. To promote the growth of the shell over the core, it may prove advantageous to choose two zeolite structures with different Si/Al but with the same framework type. Therefore, we chose to prepare binderless core-shell beads with a ZSM-5 core and a Silicalite-1 shell (both with MFI framework). This combination was previously reported for zeolites in powder format [29–34]. By coating a ZSM-5 powder (Si/Al = 34) with a shell consisting of Silicalite-1 (an all-silica zeolite), the water vapour adsorption capacity decreased from 4.96 mmol/g for ZMS-5 powder to 0.56 mmol/g for the core-shell material (Si/Al = 55) at saturated water vapour pressure (7.4 kPa at 40 °C) [34]. At the same time, the CO_2 adsorption capacity only decreased from 1.7 mmol/g to 1.5 mmol/g.

The synthesis of binderless core-shell beads with a ZSM-5 core and a Silicalite-1 shell is demonstrated here for the first time. Other types of macroscopic core-shell beads were reported before and comprised a BEA core and a thin MFI shell [35]. More recently, binderless zeolite NaX beads were coated with an NaA film to increase the CO_2/CH_4 and CO_2/N_2 selectivity [36]. Our ZSM-5/Silicalite-1 core-shell beads are the first example of binderless, macroscopically-shaped CO_2 adsorbents designed with the target of decreasing the hydrophilicity of the material while maintaining suitable CO_2 adsorption capacity. This combination of properties is highly desirable for the adsorption of CO_2 from water-containing streams.

2. Experimental

2.1. Materials

Amberlite IRA-900 in chloride form (particle size 650–820 μm), ammonium fluoride (NH_4F, ≥95%), fumed silica (SiO_2), silica gel (SiO_2, high purity grade, 230–400 mesh particle size), sodium aluminate ($NaAlO_2$), tetrapropylammonium bromide (TPABr, 98%), tetrapropylammonium hydroxide (TPAOH, 1 M in H_2O) were purchased from Sigma-Aldrich. Commercial ZSM-5 powder was obtained from Zeolyst. The H_2O used in this work was always MilliQ grade.

2.2. Methods

The synthesis method of the binderless ZSM-5 beads was developed by adapting a previously reported synthesis protocol for ZSM-5 powder [37] to include the use of Amberlite IRA-900 resin beads as hard template [28]. In a typical synthesis, 20.24 g TPAOH (1 M in H_2O) and 4.58 g SiO_2 were added to a 100 mL beaker, and the resulting mixture was stirred at 500 rpm using a magnetic stirring bar. The mixture was heated to 95 °C to promote dissolution of SiO_2. Once the mixture reached 95 °C, the heating was turned off and the mixture was stirred for 1 h. Meanwhile, 0.64 g of $NaAlO_2$ was dissolved in 10.7 g deionized H_2O by stirring for 10 min at 500 rpm. The aluminate solution was then added drop-wise over 10 min to the silicate mixture, and the resulting silicoaluminate mixture was stirred for 1 h. Then, the reaction mixture was transferred into the Teflon liner of a 100 mL stainless steel autoclave, after which 1.81 g of Amberlite IRA-900 resin beads were added while stirring. The autoclave was placed in an oven for the static hydrothermal crystallization at 150 °C for 6 d. Next, the autoclave was allowed to cool down to room temperature, after which the product mixture was filtered over a Büchner funnel and washed with 1 L of deionized H_2O. The resulting product was a mixture of zeolite powder and composite beads consisting of the Amberlite resin filled with zeolite crystallites. The beads were separated from the powder fraction by sieving. The beads and the powder fraction were calcined using the following programme: heating 3 °C/min to 200 °C, 6 h at 200 °C, heating 2 °C/min to 600 °C, 6 h at 600 °C. This method yielded 0.50 g ZSM-5-containing beads and 3.08 g ZSM-5 powder.

The ZSM-5 beads were subsequently coated with a Silicalite-1 shell, following a previously reported fluoride-assisted synthesis (in which the fluoride medium is aimed at decreasing the presence of silanol nests and, therefore, the hydrophilicity) [34]. For preparing Sil-ZSM-A, the calcined ZSM-5 beads were used, while for preparing Sil-ZSM-B the calcination step in the synthesis of the ZSM-5 beads was skipped. Briefly, 0.56 g NH_4F (important safety note: this is a particularly toxic chemical, consult safety data sheet before using) and 0.55 g TPABr were dissolved in 9.9 g deionized H_2O in the Teflon liner of a 100 mL stainless steel autoclave. Subsequently, 1.0 g fumed SiO_2 was added and the mixture was stirred for 2 h at 500 rpm using a magnetic stirring bar. 0.25 g ZSM-5 beads (for Sil-ZSM-A) or 1.0 g uncalcined ZSM-5 beads (for Sil-ZSM-B)

were added and the reaction mixture was carefully stirred at 200 rpm until the beads were homogenously distributed in the gel (about 1 min). The autoclave was then placed in an oven for the static hydrothermal crystallization at 180 °C for 90 h. After allowing to cool down to room temperature, the reaction mixture was filtered over a Büchner funnel, and the solids were washed with 1 L of deionized H_2O. The resulting product was of a mixture of Silicalite-1 powder and core-shell beads consisting of a core of ZSM-5 and a shell of Silicalite-1. The solid mixture was sieved to separate the beads from the powder fraction. The beads and the powder fraction were calcined using an air flow at 650 °C for 15 h with a heating rate of 1.2 °C/min. Yields of the bead and the powder fraction for Sil-ZSM-A and Sil-ZSM-B are given in Table 1.

2.3. Characterization

Powder X-ray diffraction (PXRD) measurements were performed on a Bruker D8 Advance apparatus with Cu Kα1 radiation (λ = 1.5418 Å) under 40 kV and 40 mA. Before performing the XRD measurements, the beads were ground into a powder using mortar and pestle. Samples were measured in the range 5–60° with a step size of 0.02 °. The slit-width was 2 mm. X-ray fluorescence (XRF) was used to perform elemental analysis of the materials. The samples were measured in plastic cups with 6 μm mylar film supporting the sample in an Epsilon 3^{XLE} spectrometer from PANalytical. Quantification was performed using the fundamental parameters method. The elements were assumed to be in their oxide forms and the sum of the obtained concentrations was normalized to 100%. The Si/Al ratio of the beads was also determined using Inductively Coupled Plasma - Atomic Emission Spectroscopy (ICP-AES) analysis. Prior to the analysis, the beads were ground and dissolved in aqueous solutions of HNO_3 (1.3%) and HF (40%). The obtained samples were measured on a PerkinElmer Optima 7000 DV optical emission spectrometer. Thermogravimetric analysis (TGA) was used to determine whether the polymer template was completely removed from the zeolitic beads upon calcination. A PerkinElmer thermogravimetric analyzer (TGA 4000) was used for the measurements. About 2 mg of ground beads was used for each analysis. The samples were heated in air from 35 to 900 °C with a heating rate of 10 °C/min. Carbon elemental analysis was used to determine whether residual carbon was present in the zeolitic beads after calcination. Combustion experiments with oxygen were conducted on an Elementar Vario Micro Cube organic elemental analyzer. Nitrogen physisorption measurements were performed at −196 °C using a Micromeritics ASAP 2420 system. The specific surface area was calculated using the Brunauer-Emmet-Teller (BET) approach. The Barrett-Joyner-Halenda (BJH) model (from the desorption branch) was used to calculate the pore size distribution and the meso- and macropore volume. The micropore volume was calculated using the t-Plot method. A VHX-7000 Keyence digital microscope was used to calculate the average bead size from a sample size of 110 beads. The obtained bead size was reported as the average diameter (mm) ± standard deviation (mm). Scanning electron microscopy (SEM) images were taken using a FEI Nova-Nano SEM 650 apparatus and were used to determine the surface morphology of the beads. The beads were coated with a 20 nm gold layer to increase image quality. A Micromeritics ASAP 2020 apparatus was used to measure the CO_2 and CH_4 adsorption isotherms. The measurements were performed at room temperature (24 °C). Before each test, the samples were degassed under vacuum at 350 °C for 10 h to remove H_2O and other possible adsorbates. Water vapour adsorption isotherms were measured by Delft Solid Solutions using a Hiden IGASorp-HT gravimetric analyzer. The sample was placed in the instrument and a gas flow of pure N_2 was applied. Prior to the measurement, the samples were pretreated at 350 °C until a stable mass was obtained in order to remove any adsorbed contaminants. The sample was step-wise subjected to increased specific relative humidity from 0 to 95% (the step size was 5% relative humidity). Mechanical strength measurements of the beads were carried out on an Instron 4301 compression tester with a maximum load of 1 kN. A stainless steel sample holder was filled with a small bed of adsorbent. During the compression test, the piston (which fits exactly in the sample holder) moved with a rate of 2 mm/min and crushed the bed until it reached the maximum load (1 kN). The load at break is divided by the surface area of the adsorbent bed to determine the mechanical strength of the bed (see Supplementary Information for further details).

Table 1
Yields of Sil-ZSM-A and Sil-ZSM-B beads and their powder side products.

Sample	Yield beads (g)	Yield powder (g)
Sil-ZSM-A	0.37	0.68
Sil-ZSM-B	0.61	0.88

3. Results and discussion

Two different types of core-shell zeolitic beads (Sil-ZSM-A and Sil-ZSM-B beads) were synthesized with the purpose of improving the hydrophobicity of the parent ZSM-5 beads, thus generating materials that are more suitable for application as CO_2 adsorbents with real gas streams, which almost invariably contain H_2O that would compete with CO_2 for the adsorption sites. Silicalite-1 was chosen as material for the shell, because this zeolite has the same framework type as the ZSM-5 crystals constituting the beads, and this is expected to facilitate the growth of the shell over the core. The obtained core-shell beads were characterized by XRD, XRF, ICP-AES, TGA, SEM and N_2 physisorption. The applicability of the beads for CO_2 adsorption was investigated and subsequently the hydrophobicity of the beads was evaluated using water vapour adsorption isotherms.

3.1. Synthesis and characterization of the zeolitic core-shell beads

The synthesis of the core-shell beads consisted of two steps: (i) synthesis of ZSM-5 in bead format, and (ii) synthesis of the Silicalite-1 shell around the ZSM-5 bead. For the synthesis of the ZSM-5 beads, Amberlite resin beads were used as a hard template. These anion-exchange resin beads shape the material in a macroscopic bead format and generate a network of meso- and macropores connecting the zeolite crystals (Fig. 1 and Fig. S1), thus engendering a hierarchical porous structure in which the zeolitic micropores are accessed through larger pores [19–21]. Two alternative strategies have been used to synthesize two different core-shell beads. The first step in the synthesis of the core-shell beads, i.e. the synthesis of the ZSM-5 in bead format, is the same for both routes. In the basic reaction mixture, negatively charged zeolite oligomers are formed which can exchange with the anions of the Amberlite resin. Condensation and crystallization of the oligomers during the hydrothermal crystallization yielded polymer beads filled with zeolite crystallites. Part of the oligomers did not diffuse into the Amberlite beads but remained in solution, and these crystallized to yield ZSM-5 zeolite in powder form as a side product. In route A, the polymer-zeolite composite was calcined, and by burning off the polymer an interconnected network of meso- and macropores was generated within the ZSM-5 beads (Fig. 1). Subsequently, a shell of Silicalite-1 was synthesized around the ZSM-5 beads, yielding Sil-ZSM-A core-shell beads. For this route, the challenge was to prevent Silicalite-1 to fill the meso- and

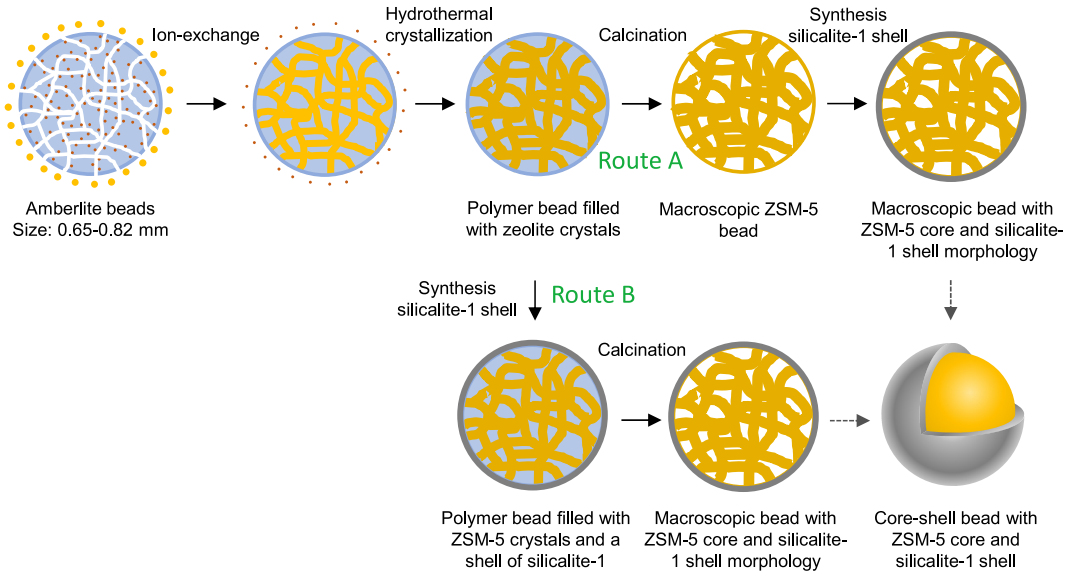

Fig. 1. Schematic representation of the synthetic routes used to prepare the core-shell zeolitic beads.

macroporous network present inside the ZSM-5 beads. This risk is intrinsically avoided in route B (Fig. 1), in which the Silicalite-1 shell was synthesized around the as-prepared polymer-zeolite composite and only afterwards the beads were calcined. The presence of the polymer template during the synthesis of the Silicalite-1 shell prevents the formation of Silicalite-1 within the bead. Subsequent calcination of the beads should generate the desired network of meso- and macropores within these Sil-ZSM-B core-shell beads. However, it may be challenging to fully remove the Amberlite template if the shell of the beads is too thick or not porous enough. Based on these considerations, each synthetic strategies has advantages and possible limitations, and thus deserved being investigated. This approach yielded two different materials in bead format (Sil-ZSM-A beads and Sil-ZSM-B beads). In both routes, during the synthesis of the Silicalite-1 shell, not all of the Silicalite-1 was formed around the beads but part of the Silicalite-1 was formed in powder form as a side product (Sil-ZSM-A pow and Sil-ZSM-B pow). For route A, the yield of the beads was 35% of the total yield and for route B the yield of the beads was 41% (see also Table 1).

The Sil-ZSM-A and Sil-ZSM-B beads were investigated by SEM to determine whether the desired core-shell format was obtained. Indeed, from the SEM images (Fig. 2C, Fig. 2G and H) it can be clearly seen that a core-shell structure was obtained for both Sil-ZSM-A and Sil-ZSM-B beads as the exterior and the interior of the beads presented different crystal morphologies. Though both beads displayed the desired core-shell structure, their physicochemical properties differed significantly. For the Sil-ZSM-B beads, the interior of the beads consists of more or less spherical aggregates of small crystals (Fig. 2H and I), while the shell consists of thin, elongated hexagonal crystals (Fig. 2J and K). That fact that this shell consists of the desired Silicalite-1 phase is supported by the SEM images of Silicalite-1 powder, which display similar elongated hexagonal crystals whereas the ZSM-5 powder consists of small, more or less spherical crystals (Fig. S2). For the Sil-ZSM-A beads, the exterior also consists of elongated hexagonal crystals (Fig. 2E), but the interior consists of larger crystals (Fig. 2D) compared to those in the ZSM-5 powder (Fig. S2) or in the interior of the ZSM-5 beads (Fig. S1) and Sil-ZSM-B beads. Besides being larger, the crystals in the interior of Sil-ZSM-A also present the thin hexagonal structures that are characteristic of Silicalite-1 (Fig. 2D). This suggests that not only the exterior of the bead, but also part of the ZSM-5 interior crystals was coated by Silicalite-1 crystals. This was only observed for the Sil-ZSM-A beads and not for the Sil-ZSM-B beads because during the synthesis of the Silicalite-1 layer, the Sil-ZSM-B beads still contained the Amberlite template, which prevented the Silicalite-1 crystals from growing in the interior of the beads. Additionally, the shell of the Sil-ZSM-A beads seems thicker compared to that of the Sil-ZSM-B beads (Fig. 2C and H). This is supported by the average bead size of the different materials: the average size of the Sil-ZSM-B beads (0.73 ± 0.14 mm) is similar to that of the parent ZSM-5 beads (0.74 ± 0.15 mm, see Fig. S1), while the size of the Sil-ZSM-A beads is clearly larger (0.84 ± 0.12 mm). The difference between Silicalite-1 and ZSM-5 cannot be observed by XRD since they both possess the MFI framework. The parent ZSM-5 beads displayed all the characteristic peaks representing the MFI framework, and additionally a broad peak centred at 23° corresponding to an amorphous silica/aluminosilicate phase. The intensity of the peaks representing the MFI framework increased after adding the Silicalite-1 shell and no new peaks were observed, indicating that the shell layer completely consists of the MFI framework (Fig. 3). For both the Sil-ZSM-A and Sil-ZSM-B beads, the surface of the beads was not completely covered by a Silicalite-1 shell, but defects were observed (Fig. 2C, G, H). Additionally, for both the Sil-ZSM-A and Sil-ZSM-B beads, some overgrown crystals were observed on the surface of the beads (Fig. 2A, B, F, G), with such overgrowth phenomenon being more common and more pronounced for the Sil-ZSM-A beads.

The Si/Al ratio of the beads was determined by XRF and ICP-AES analysis and that of the powders was determined only by XRF analysis (Table 2, full chemical compositions in Table S1). Though the Si/Al values of the beads obtained by XRF and ICP-AES showed some degree of discrepancy (particularly in the case of Sil-ZSM-B beads), the trend in Si/Al ratio between the materials is the same with the two techniques. Since the Silicalite-1 used for the shell is an all-silica zeolite, an increase in Si/Al ratio is expected in the final core-shell material compared to the parent ZSM-5 beads. Indeed, the Si/Al ratio of the Sil-ZSM-A beads (57 based on XRF, 50 based on ICP-AES) and Sil-ZSM-B beads (27 based on XRF, 18 based on ICP-AES) are both higher than that of the parent ZSM-5 beads (13 based on XRF, 15 based on ICP-AES), indicating that the shell formed around the ZSM-5 beads contains low amounts of aluminium and is

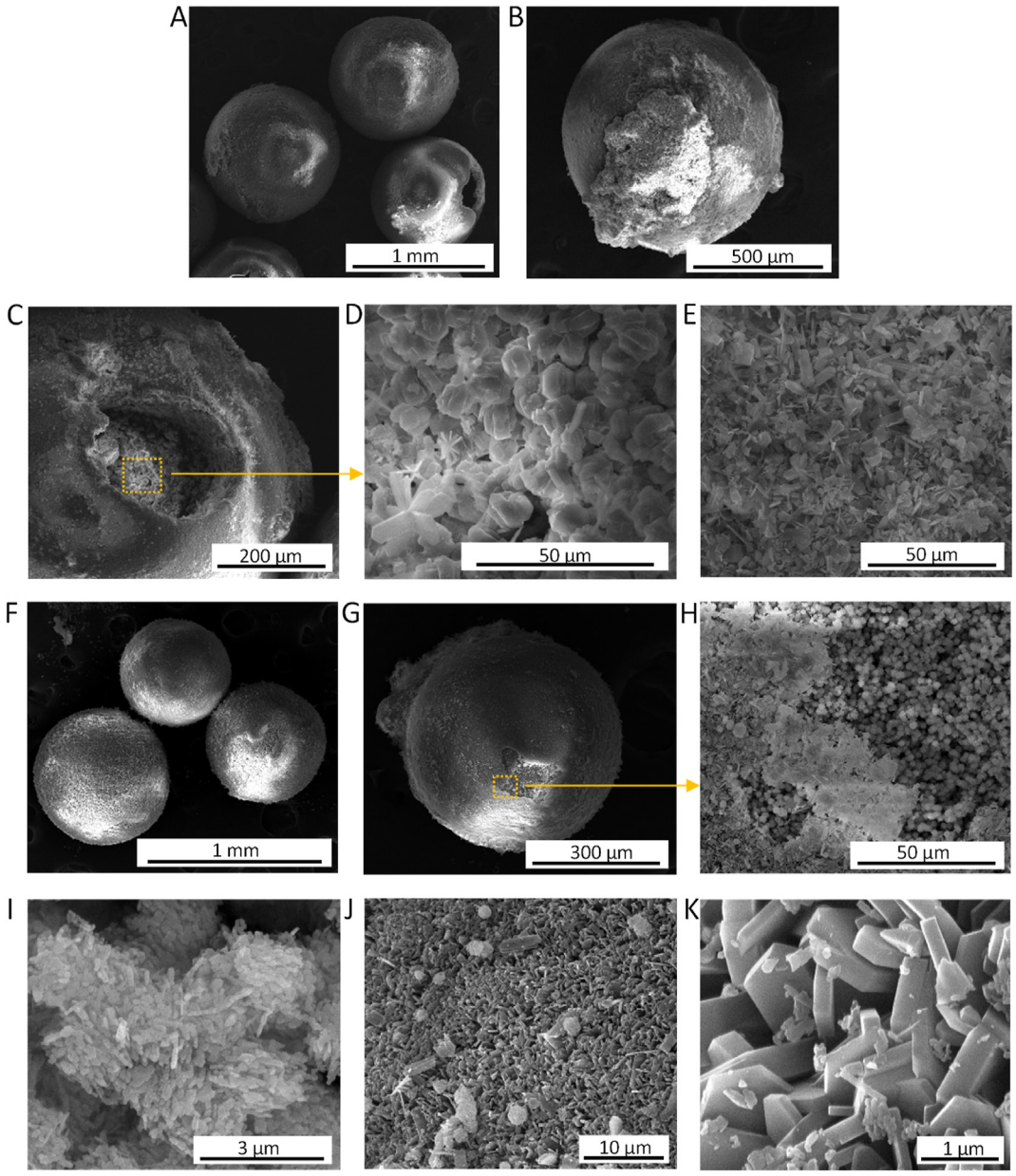

Fig. 2. SEM images of Sil-ZSM-A beads (A), Sil-ZSM-A bead with significant overgrowth (B), Sil-ZSM-A bead with a hole in the shell (C) through which the interior of a Sil-ZSM-A bead (D) can be visualized, shell of a Sil-ZSM-A bead (E), Sil-ZSM-B beads (F), Sil-ZSM-B bead with a hole in the shell (G) and magnification of the hole area (H), interior of a Sil-ZSM-B bead (I), shell of a Sil-ZSM-B bead (J, K).

thus expected to be hydrophobic. The Si/Al ratio of Sil-ZSM-A beads is higher than that of the Sil-ZSM-B beads, which is attributed to the observed coating of the interior of the Sil-ZSM-A beads by Silicalite-1 and to the thicker shell and more prominent overgrowth observed for the Sil-ZSM-A beads compared to the Sil-ZSM-B beads (*vide supra*). For the same reasons, the mechanical strength of the Sil-ZSM-A beads (0.31–2.69 MPa) was higher than that of the Sil-ZSM-B beads (0.20–1.16 MPa, see Figs. S3–S5 and Table S2 for more information). Yet, the thinner shell of the Sil-ZSM-B beads still led to enhanced mechanical strength compared to the parent ZSM-5 beads (0.16–0.87 MPa). The ZSM-5 beads displayed comparable mechanical strength to LTA beads (0.14–0.82 MPa) synthesized using a similar hard-templating method and for which it was calculated that they should be strong enough to be used in an industrial process (with an adsorption column that is 3 m high and 1 m in diameter) without suffering significant deterioration [19]. Thus, the core-shell beads, having enhanced mechanical stability compared to the ZSM-5 and LTA beads, are expected to display suitable mechanical strength for large scale application.

It should be noted that the ZSM-5 beads were synthesized in their H-form and, therefore, both core-shell zeolites are also in their H-form (Table S1). For application as CO_2 adsorbents, the extra-framework cations may be exchanged with Na^+ or other alkali, alkaline earth, transition or rare earth metals to optimize the adsorption behaviour (e.g. adsorption capacity, enthalpy of adsorption or cyclic adsorption performance) for a specific separation process [38].

The powder side products obtained in the synthesis of Sil-ZSM-A and Sil-ZSM-B beads are expected to have the same composition as the shell and are thus expected to be Silicalite-1. Indeed, XRD

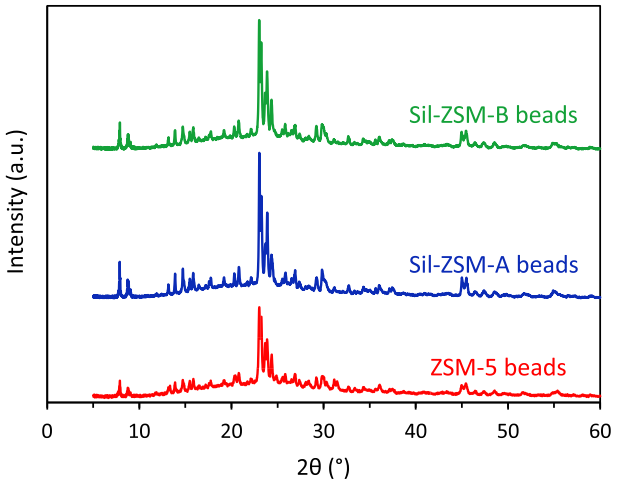

Fig. 3. XRD pattern of ZSM-5 beads, Sil-ZSM-A beads and Sil-ZSM-B beads.

analysis of the powders indicated that they consist of an MFI framework (Fig. S6). While Sil-ZSM-B pow is an all-silica material and is thus Silicalite-1, Sil-ZSM-A pow also contains a small amount of aluminium (Table 2, full chemical compositions in Table S3) and is thus a Si-rich ZSM-5 rather than a Silicalite-1. It is likely that some aluminium (and possibly also silicon) from the ZSM-5 beads was dissolved during the hydrothermal crystallization due to the relatively harsh reaction conditions, and that these Al atoms were incorporated in the powder product. Another possibility is that some of the beads may have been broken due to the agitation with the magnetic stirrer, which resulted in the presence of some ZSM-5 in the powder fraction. These issues are unlikely to happen during the hydrothermal synthesis of the Sil-ZSM-B beads, as the Amberlite template is still present around the ZSM-5 parent beads, thus preventing leaching of Al into the reaction mixture and providing additional mechanical strength to the beads, making them more resistant to the agitation of the magnetic stirring bar. This explains why the powder side product, Sil-ZSM-B pow, is a Silicalite-1 structure.

N_2 physisorption isotherms of the core-shell beads show that while all beads possess microporosity (as observed from the sharp increase at low relative pressure $p/p^0 < 0.05$) and meso- and/or macroporosity (as observed from the hysteresis at higher relative pressure $p/p^0 > 0.45$), the meso- and macroporosity of the Sil-ZSM-A beads and Sil-ZSM-B beads differ significantly (Fig. 4). While the N_2 physisorption isotherm of the Sil-ZSM-B beads had analogous features to those of the ZSM-5 beads, the isotherm for the Sil-ZSM-A beads was notably different. For the Sil-ZSM-A beads, the Amberlite resin was removed before the synthesis of the Silicalite-1 shell. Therefore, it is likely that while we aimed to form only a shell around the bead, part of the Silicalite-1 was also formed within the meso- and macropores of the parent ZSM-5 bead (*vide supra*). The presence of Silicalite-1 within the pores of the Sil-ZSM-A beads significantly decreased the meso- and macropore volume and the pore width compared to the parent ZSM-5 beads (Table 2 and Fig. 4). In the pore size distribution for the Sil-ZSM-A and Sil-ZSM-B beads (Fig. 4), a peak around 2 nm is observed. However, this is not caused by an actual porosity but to a transition of the adsorbed N_2 between a disordered "fluid" phase to a more ordered "crystalline" phase [39]. This behaviour is characteristic of materials with a Si/Al > 100 (as the Silicalite-1 shell) [39]. Indeed, this feature is more pronounced for Sil-ZSM-A pow and Sil-ZSM-B pow, as they possess a higher Si/Al ratio (Fig. S7). The N_2 adsorption isotherm of the Sil-ZSM-A beads furthermore displays a tensile strength effect (TSE) around $p/p^0 = 0.45–0.5$, which leads to an artefact peak at 4 nm in the pore size distribution (Fig. 4). At this partial pressure, the hysteresis due to capillary condensation in meso- and/or macropores undergoes a forced closure due to instability of the hemispherical meniscus during desorption [40]. The impact of this TSE becomes larger when pore network effects occur, i.e. when large pores are connected to the outer surface of the material through smaller pores. This suggests that the beads possess so-called ink-bottle pores, i.e. the interior of the Sil-ZSM-A beads still contains relatively large pores, but their openings giving access the surface of the bead are probably restricted by the formation of Silicalite-1 in the pores. The Sil-ZSM-B beads displayed a very similar N_2 adsorption isotherm to the parent ZSM-5 beads, because for both materials the last step of the synthesis was the calcination of the Amberlite template, which generates a network of meso- and macropores. The pore volume of the Sil-ZSM-B beads was therefore only slightly lower than that of the ZSM-5 beads (Table 2, Fig. 4). The presence of the Amberlite template during the synthesis of the Silicalite-1 shell is thus crucial for obtaining a core-shell bead with similar porosity to that of the pristine ZSM-5 beads.

The meso- and macroporosity of the zeolitic beads originates from the removal of the resin beads used as hard template. To investigate whether the template was completely removed during calcination, TGA of the zeolitic beads was performed (Fig. S8). This analysis showed a small percentage of mass loss (<10%) upon heating the samples from 35 to 900 °C. All samples showed a relatively rapid mass decrease up to about 200 °C, which likely stems from removal of physisorbed water from the zeolitic beads. It is worth noting that the mass loss attributed to removal of physisorbed water is more significant for the ZSM-5 beads than that observed for the Sil-ZSM-A and Sil-ZSM-B beads, suggesting that the core-shell beads display the desired lower hydrophilicity. If the calcination were not sufficient to completely remove the template, another significant mass decrease would be expected at high temperatures (around the calcination temperature, 650 °C). However, at high temperatures no significant weight loss was observed, indicating that the template removal was successful using the employed calcination method. This conclusion was further supported by carbon elemental analysis, which indicated that virtually no carbon was present in any of the calcined bead materials (Table S4).

3.2. Application of the beads for CO_2 adsorption

The applicability of the Sil-ZSM-A and Sil-ZSM-B beads for CO_2 adsorption in the context of biogas upgrading was investigated by measuring the CO_2 and CH_4 adsorption capacities at room temperature in the 0–1 bar range. Their adsorption behaviour was compared to that of ZSM-5 beads, commercial ZSM-5 powder and Silicalite-1 powder (Sil-ZSM-B pow) (Fig. 5 and Table 3). The CO_2 adsorption capacity of the Sil-ZSM-B beads (2.00 mmol/g at 1 bar, 1.3 mmol/g at 0.4 bar, i.e. the partial pressure of CO_2 in 1 bar biogas) is slightly higher than that of the Sil-ZSM-A beads (1.94 mmol/g at 1 bar, 1.25 mmol/g at 0.4 bar), and both beads display slightly lower CO_2 adsorption capacity compared to the parent ZSM-5 beads (2.13 mmol/g at 1 bar, 1.60 mmol/g at 0.4 bar). In general, the CO_2 adsorption behaviour can be rationalized based on the number of accessible cation sites in the zeolitic framework acting as adsorption sites, which in turn is related to the Al-content, the degree of crystallinity and the accessible surface area and micropore volume of the beads [19]. Although the degree of crystallinity of the Sil-ZSM-A beads and Sil-ZSM-B beads is slightly higher than that of the parent ZSM-5 beads, this difference is mainly caused by the Silicalite-1 phase in the former two materials. Since Silicalite-1 contains no or negligible amount of Al and thus of cation sites, the higher crystallinity stemming from this phase is not expected to

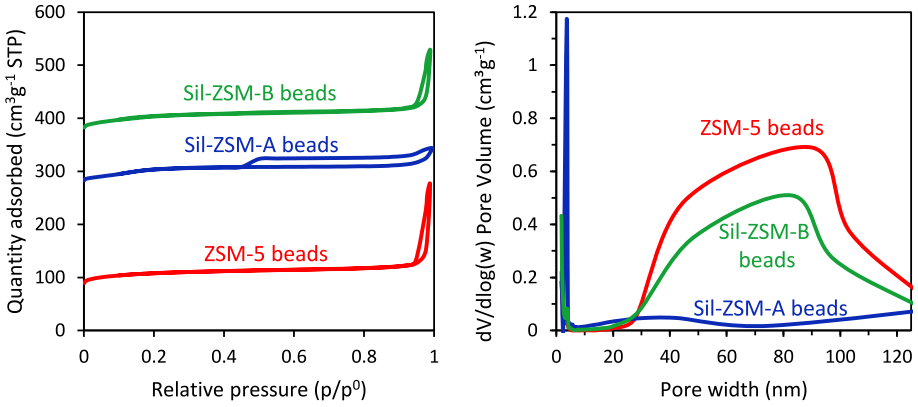

Fig. 4. N_2 physisorption isotherms (left) and pore size distribution (right) for ZSM-5, Sil-ZSM-A and Sil-ZSM-B beads. The N_2 physisorption isotherm of Sil-ZSM-A and Sil-ZSM-B beads are shifted upwards by 200 and 300 cm^3/g, respectively, to facilitate their visualization.

Table 2
Physicochemical properties of ZSM-5, Sil-ZSM-A and Sil-ZSM-B beads and powders.

Material	BET surface area (m^2/g)	Micropore volume (cm^3/g)	Meso- and macropore volume (cm^3/g)	Si/Al (XRF)[b]	Si/Al (ICP)[c]
ZSM-5 beads	383	0.13	0.29	13	15
ZSM-5 pow	261	0.10	0.06[a]	8.7	
Sil-ZSM-A beads	365	0.08	0.13	57	50
Sil-ZSM-A pow	399	0.06	0.04[a]	70	
Sil-ZSM-B beads	365	0.10	0.24	27	18
Sil-ZSM-B pow	384	0.02	0.15[a]	∞	

[a] These materials have no structural meso- and macropores (see Fig. S2). Therefore, the volume in the meso- and macropore range should be attributed to non-structural interparticle voids.
[b] Determined by XRF analysis.
[c] Determined by ICP-AES analysis.

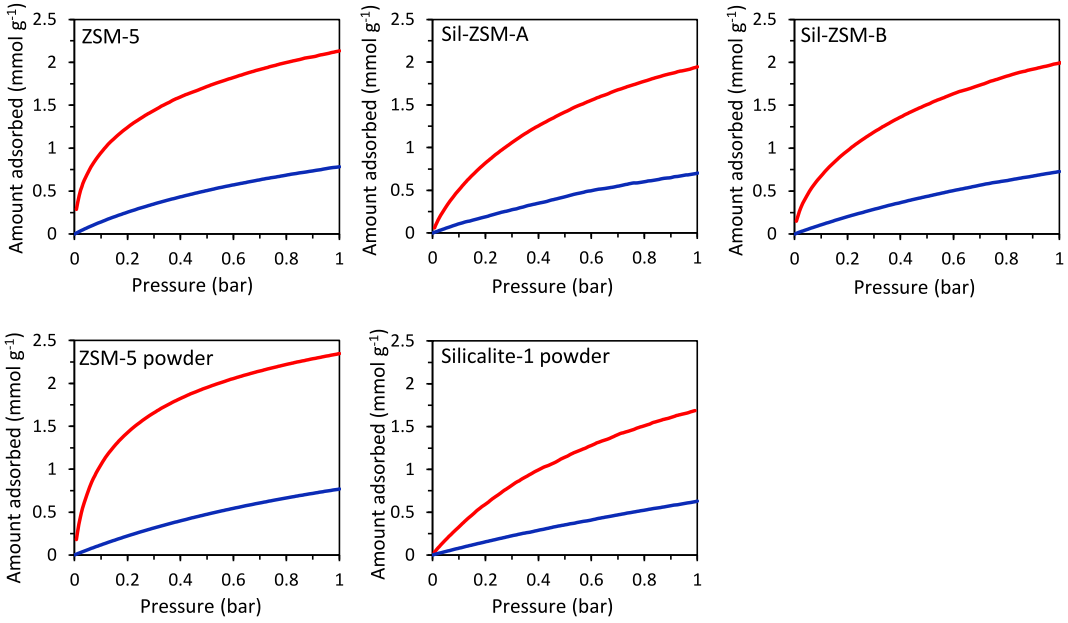

Fig. 5. CO_2 (red) and CH_4 (blue) adsorption isotherms at 25 °C for ZSM-5, Sil-ZSM-A and Sil-ZSM-B beads and for ZSM-5 (commercial) powder and Silicalite-1 powder.

contribute to the CO_2 adsorption capacity. Therefore, the observed slightly lower CO_2 adsorption capacity of the core-shell beads compared to the parent ZSM-5 beads can be attributed to their Si/Al ratios (Table 2), as zeolites with a lower Si/Al ratio possess more cation sites that function as the adsorption sites for CO_2 [41]. It should be noted that the measured Si/Al ratio is that of the whole beads, which consist not only of zeolitic MFI phases, but also of an amorphous silica/aluminosilicate phase. Therefore, the Si/Al ratio of the zeolitic phases is not necessarily the same as that of the whole beads. However, XRD analysis indicated that the amorphous phase originated from the synthesis of the ZSM-5 parent beads and that the addition of the Silicalite-1 shell did not increase the intensity of

Table 3
CO_2, CH_4 and H_2O adsorption capacities and CO_2/CH_4 selectivity for ZSM-5, Sil-ZSM-A and Sil-ZSM-B beads and for ZSM-5 and Silicalite-1 powders.

Material	CO_2 adsorption capacity (mmol/g)		CH_4 adsorption capacity (mmol/g)		CO_2/CH_4 selectivity[a]	H_2O adsorption capacity (mmol/g)	
	at 1 bar CO_2	at 0.4 bar CO_2	at 1 bar CH_4	at 0.6 bar CH_4		at 5% RH[b]	at max RH[b]
ZSM-5 beads	2.13	1.60	0.78	0.57	4.3	2.90	5.83
Sil-ZSM-A beads	1.94	1.25	0.70	0.49	3.8	1.67	4.18
Sil-ZSM-B beads	2.00	1.36	0.71	0.51	4.1	2.37	5.39
ZSM-5 powder (commercial)	2.35	1.82	0.77	0.55	5.1	3.61	5.92
Silicalite-1 powder (Sil-ZSM-B pow)	1.69	0.99	0.63	0.41	3.7	0.48	1.20

[a] The CO_2/CH_4 selectivity is calculated using $s = (q_{CO_2}/q_{CH_4})/(p_{CO_2}/p_{CH_4})$, in which q is the adsorption capacity of a compound (CO_2 or CH_4) at its partial pressure p in the hypothetical gas mixture. The partial pressure of CO_2 is 0.4 and that of CH_4 is 0.6.
[b] RH = relative humidity.

the amorphous phase (Fig. 3). Therefore, the increased Si/Al ratio after the addition of the Silicalite-1 shell only originates from an increase in zeolitic phase. This means that the differences in the Si/Al ratios between Sil-ZSM-A and Sil-ZSM-B beads and the parent ZSM-5 beads can be used to rationalize the observed differences in their CO_2 adsorption capacity. The Sil-ZSM-A and Sil-ZSM-B beads both displayed higher adsorption capacity compared to the Silicalite-1 powder (Table 3), which is expected based on their Si/Al ratio. While Sil-ZSM-A and Sil-ZSM-B contain cation sites that can act as adsorption sites for CO_2, all-silica zeolites as Silicalite-1 do not contain cation sites and CO_2 can only adsorb on the oxygen atoms of the zeolite framework, leading to lower CO_2 adsorption capacity [11]. While the lack of cation sites due to the all-silica nature of the Silicalite-1 powder can explain its lower adsorption capacity, this effect was probably partially counterbalanced by its higher degree of crystallinity (see Fig. S6). Typically, the degree of crystallinity of zeolitic beads is lower than that of zeolites in powder format and, therefore, zeolitic beads display (slightly) lower CO_2 adsorption capacity [19]. In line with these observations, the ZSM-5 beads displayed lower CO_2 adsorption capacity compared to a commercial ZSM-5 powder with a similar Si/Al ratio (Table 3; see Fig. S9, Fig. S10, Tables S3 and S5 for XRD, XRF and N_2 physisorption data).

It is worth noting that all materials discussed so far were in their H-form, which means that their CO_2 adsorption behaviour can be further optimized by ion-exchange. For example, partial ion-exchange of the commercial ZSM-5 powder by Na^+ (Na/Al = 0.46) increased the CO_2 adsorption capacity from 2.35 mmol/g (H-form) to 2.60 mmol/g at 1 bar CO_2. However, optimizing the nature of the counter-cation for all the studied materials is outside the scope of this work, which focuses on investigating the effect of the core-shell structure on the control of the hydrophobicity of the zeolitic beads.

The shape of the CO_2 adsorption isotherm of Silicalite-1 powder was considerably different from that of ZSM-5 powder (Fig. 5), with ZSM-5 powder displaying a steeper increase in the adsorption isotherm at low relative pressure (<0.1 bar). This corresponds to a higher enthalpy of adsorption and stems from the presence of cation sites in ZSM-5, which are known to have relatively strong interaction with CO_2 [11]. For Silicalite-1, the interaction with CO_2 is less strong since there are no or very little cation sites and CO_2 can only adsorb on the oxygen atoms of the zeolite framework, which have a relatively weak interaction with CO_2 [11]. The Sil-ZSM-A and Sil-ZSM-B beads display an isotherm with an intermediate steepness between that of the Silicalite-1 and ZSM-5 powders (Fig. 5), in agreement with the fact that these materials contain both a ZSM-5 (core) and a Silicalite-1 (shell) phase.

For the ZSM-5, Sil-ZSM-A and Sil-ZSM-B beads and the ZSM-5 and Silicalite-1 powder, CH_4 adsorption isotherms were measured (Fig. 5, Table 3). The highest CH_4 adsorption capacity at 0.6 bar and 1 bar was observed for the ZSM-5 beads (0.57 mmol/g and 0.78 mmol/g, respectively) and the lowest for Silicalite-1 powder (0.41 mmol/g and 0.63 mmol/g, respectively). Similarly to the CO_2 adsorption capacity, the presence of cations in ZSM-5 and the lack of cations in Silicalite-1 also affect the CH_4 adsorption capacity, as CH_4 preferentially interacts with the cation-site of the zeolite [42,43]. It is thus in line with logical expectations that both core-shell beads display CH_4 adsorption capacities between those of ZSM-5 and Silicalite-1. The CO_2/CH_4 selectivity was calculated for all materials (Table 3) and was slightly higher for the materials with a lower Si/Al ratio, and thus with a steeper adsorption isotherm.

The core-shell structure envisaged for the Sil-ZSM-A and Sil-ZSM-B beads was aimed at providing a hydrophobic barrier to prevent H_2O from reaching the adsorption sites in the ZSM-5 structure. To check the effectiveness of our strategy, the hydrophobicity of the Sil-ZSM-A and Sil-ZSM-B beads was evaluated by single-component water vapour adsorption isotherms, and these were compared with the water vapour adsorption isotherms of the parent ZSM-5 beads, and of ZSM-5 and Silicalite-1 powder (Fig. 6, Table 3). For all materials, the adsorption of H_2O was relatively more substantial at low relative humidity (RH, 5%), while at higher RH a relatively low additional amount of H_2O was adsorbed (Fig. 6). This corresponds to a type I isotherm, which represents the adsorption of H_2O into micropores and/or a strong interaction of H_2O with the sample surface. While the shape of the H_2O adsorption isotherms is similar for the different materials, there are clear differences among them in terms of total H_2O adsorption. As expected, the Silicalite-1 powder displayed the lowest H_2O adsorption due to the hydrophobic nature of this all-silica zeolite. The

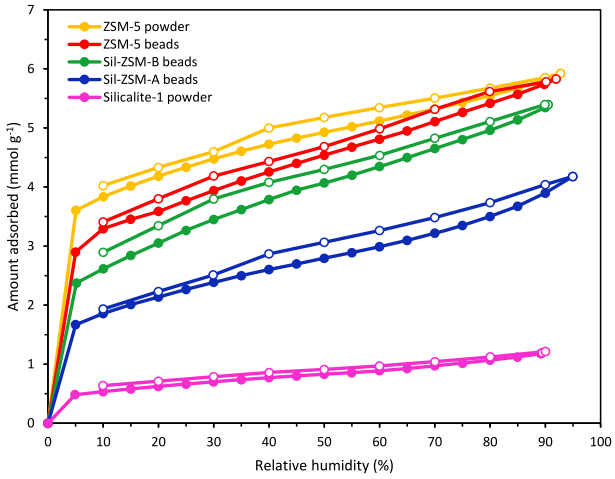

Fig. 6. Water vapour adsorption isotherms at 25 °C for ZSM-5, Sil-ZSM-A and Sil-ZSM-B beads and ZSM-5 and Silicalite-1 powder; filled circles: adsorption, open circles: desorption.

ZSM-5 beads and powder displayed the highest H_2O adsorption capacity due to their relatively low Si/Al ratio. Interestingly, the ZSM-5 beads displayed about 20% lower H_2O adsorption compared to the ZSM-5 powder at low relative humidity (5%), which could be ascribed to its slightly higher Si/Al ratio. The fact that the isotherms have a very similar maximum uptake should thus be ascribed to the larger mesopore volume of the ZSM-5 beads (due to the bead format). The Sil-ZSM-B beads displayed only slightly lower (7%) H_2O adsorption capacity compared to the ZSM-5 parent beads at maximum relative humidity. At low relative humidity (5%), the Sil-ZSM-B beads displayed a notably lower adsorption of H_2O (18%) compared to that of the parent ZSM-5 beads. At slightly higher relative humidity (20%), which is a value more relevant in CO_2 adsorption processes, the Sil-ZSM-B beads displayed a similar decrease in H_2O adsorption (15%) as observed at 5% RH. The decrease in water adsorption capacity is attributed to the hydrophobic Silicalite-1 shell that was formed around the ZSM-5 beads. For the Sil-ZSM-A beads, not only a shell was formed around the beads, but also part of the interior was coated with Silicalite-1. This ensures a more significant decrease in H_2O adsorption capacity for the Sil-ZSM-A beads compared to the parent ZSM-5 beads (42% at 5% RH, 40% at 20% RH and 28% at maximum RH). Importantly, the CO_2 adsorption capacity at 1 bar of the Sil-ZSM-A beads decreased to a much lower extent (about 9%). The lower H_2O adsorption capacity measured for the core-shell beads compared to the parent ZSM-5 beads provides a proof of principle of the effectiveness of our material design strategy. Future work should investigate the competitive adsorption between CO_2 and H_2O over the parent and the core-shell beads using a humid CO_2 gas stream in a pressure swing adsorption setup. Though the H_2O adsorption capacity of both core-shell beads was lowered compared to that of the parent ZSM-5 beads, the H_2O adsorption capacity is still significantly higher than that of Silicalite-1 powder. This is likely due to the presence of defects in the shell that was formed around the beads (see Fig. 2C, G and H). Future work can be aimed at obtaining a shell in which these defects are absent or minimized. This could be achieved by reiterating the synthesis step in which the Silicalite-1 layer is formed, resulting in a less defective shell and thus in a further decrease in H_2O adsorption capacity.

4. Conclusions

Two synthetic strategies were designed and explored to prepare novel core-shell zeolitic beads with hierarchical porosity, consisting of a core of ZSM-5 to impart CO_2 adsorption capacity and a shell of Silicalite-1 to provide hydrophobicity to the material. This combination of features is attractive for application of the zeolitic beads as adsorbents in biogas upgrading, by allowing separation of CO_2 from CH_4 through selective adsorption while minimizing the undesired competitive adsorption of H_2O. The two synthetic strategies used to prepare the core-shell beads (Sil-ZSM-A and Sil-ZSM-B) differed in the use of calcined or uncalcined ZSM-5 beads as parent material on which the Silicalite-1 shell was grown. SEM, XRF and ICP-AES analysis indicated that the desired core-shell format was achieved for both the Sil-ZSM-A and Sil-ZSM-B beads. Notably, the Silicalite-1 shell increased the mechanical strength of both core-shell beads compared to that of the parent ZSM-5 beads. Therefore, these beads have the potential to be used for industrial application without suffering significant structural degradation. For the Sil-ZSM-B beads, the presence of the polymeric template during the synthesis of the Silicalite-1 shell layer prevented the formation of Silicalite-1 in the interior of the beads and, therefore, the pristine texture of the parent ZSM-5 beads was largely retained. For the Sil-ZSM-A beads, Silicalite-1 was not only formed as a shell around the ZSM-5 beads, but also partly in the interior of the beads, leading to a lower porosity compared to the parent ZSM-5 beads and higher Si/Al ratio compared to the Sil-ZSM-B beads. Both core-shell beads were tested as adsorbents for CO_2. The CO_2 adsorption capacity of the core-shell beads (1.94 mmol/g at 1 bar for Sil-ZSM-A beads and 2.00 mmol/g at 1 bar for Sil-ZSM-B beads) was slightly lower than that of the parent ZSM-5 beads (2.13 mmol/g at 1 bar) due to their increased Si/Al ratios and, therefore, lower amount of adsorption sites per unit mass of material. On the other hand, the presence of the Silicalite-1 shell allowed enhancing the hydrophobicity of the zeolitic beads, as demonstrated by measuring their water vapour adsorption isotherms. Both core-shell beads presented the desired lower H_2O adsorption capacity compared to the parent ZSM-5 beads, with the decrease being much more significant for the Sil-ZSM-A beads (40% lower H_2O adsorption compared to ZSM-5 beads at 20% relatively humidity) than for the Sil-ZSM-B beads (15% decrease at 20% relatively humidity). This work provides a proof of concept of the effectiveness of our strategy in which a shell of hydrophobic Silicalite-1 is grown around a ZSM-5 bead core in order to reduce the H_2O adsorption capacity of the material. This strategy has the potential to be extended to other types of zeolites. In particular, for the core of the beads, other zeolites with higher CO_2 adsorption capacities (i.e. with lower Si/Al ratio than the ZSM-5 used in this work) and higher selectivity towards CO_2 would be desirable. Furthermore, this work offers an attractive and accessible method to improve the mechanical stability of binderless zeolitic beads, while preserving their hierarchical porosity.

Authors' contributions

Dina G. Boer: Writing – original draft, Visualization, Validation, Methodology, Investigation, Formal analysis, Data curation, Conceptualization. **Zahra Asgar Pour:** Methodology, Investigation. **Stefano Poli**: Investigation. **Jort Langerak:** Supervision, Project administration. **Benny Bakker:** Supervision, Project administration, Funding acquisition. **Paolo P. Pescarmona:** Writing – review & editing, Supervision, Conceptualization, Resources, Project administration, Methodology, Funding acquisition, Formal analysis, Data curation.

Funding

This work was supported by DMT Environmental Technology and Samenwerkingsverband Noord-Nederland (SNN, KEIPR003).

Declaration of competing interest

The authors declare that they have no known competing financial interests or personal relationships that could have appeared to influence the work reported in this paper.

Data availability

Data will be made available on request.

Acknowledgements

The authors acknowledge funding for the project by DMT Environmental Technology and Samenwerkingsverband Noord-Nederland (SNN, KE18PR003). We acknowledge Léon Rohrbach for analytical support and Jacob Baas for support with XRD analysis. We thank Julian Strien for his help with TGA analysis, and Hans van der Velde and Paula Ortega Araiztegi for their help with ICP-AES and carbon elemental analysis.

Appendix A. Supplementary data

Supplementary data to this article can be found online at https://doi.org/10.1016/j.mtchem.2023.101621.

References

[1] H. Ritchie, M. Roser, CO_2 and Greenhouse Gas Emissions, Publ. Online OurWorldInData.Org., 2020. https://ourworldindata.org/co2-and-other-greenhouse-gas-emissions (accessed June 2, 2022).

[2] T.J. Blasing, Recent greenhouse gas concentrations. https://doi.org/10.3334/CDIAC/atg.032, 2011.

[3] X. Wang, C. Song, Carbon capture from flue gas and the atmosphere: a perspective, Front. Energy Res. 8 (2020), https://doi.org/10.3389/fenrg.2020.560849.

[4] F.M. Baena-Moreno, M. Rodríguez-Galán, F. Vega, B. Alonso-Fariñas, L.F. Vilches Arenas, B. Navarrete, Carbon capture and utilization technologies: a literature review and recent advances, Energy Sources, Part A Recover, . Util. Environ. Eff. 41 (2019) 1403–1433, https://doi.org/10.1080/15567036.2018.1548518.

[5] International Association of Oil and Gas Producers, The potential for CCS and CCU in Europe. https://ec.europa.eu/info/sites/info/files/iogp_-_report_-_ccs_ccu.pdf, 2019.

[6] C.H. Huang, C.S. Tan, A review: CO_2 utilization, Aerosol Air Qual. Res. 14 (2014) 480–499, https://doi.org/10.4209/aaqr.2013.10.0326.

[7] E.I. Koytsoumpa, C. Bergins, E. Kakaras, The CO_2 economy: review of CO_2 capture and reuse technologies, J. Supercrit. Fluids 132 (2018) 3–16, https://doi.org/10.1016/j.supflu.2017.07.029.

[8] A.J. Kamphuis, F. Picchioni, P.P. Pescarmona, CO_2-fixation into cyclic and polymeric carbonates: principles and applications, Green Chem. 21 (2019) 406–448, https://doi.org/10.1039/c8gc03086c.

[9] M.T. Ho, G.W. Allinson, D.E. Wiley, Reducing the cost of CO_2 capture from flue gases using pressure swing adsorption, Ind. Eng. Chem. Res. 47 (2008) 4883–4890, https://doi.org/10.1021/ie070831e.

[10] D.P. Harrison, The role of solids in CO_2 capture: a mini review, Greenh. Gas Control Technol. 7 (11) (2005) 1101–1106.

[11] D.G. Boer, J. Langerak, P.P. Pescarmona, Zeolites for CO_2 adsorption, ACS Appl. Energy Mater. 6 (5) (2023) 2634–2656. https://pubs.acs.org/doi/full/10.1021/acsaem.2c03605.

[12] C. Song, W. Pan, S.T. Srimat, J. Zheng, Y. Li, Y.H. Wang, B.Q. Xu, Q.M. Zhu, Tri-reforming of methane over Ni catalysts for CO_2 conversion to Syngas with desired H2CO ratios using flue gas of power plants without CO_2 separation, Stud. Surf. Sci. Catal. 153 (2004) 315–322, https://doi.org/10.1016/s0167-2991(04)80270-2.

[13] R. Zevenhoven, P. Kilpinen, Flue Gases and Fuel Gases, Control Pollut, Flue Gases Fuel Gases, 2001, pp. 2.1–2.12. http://users.abo.fi/rzevenho/gases.PDF.

[14] I. Angelidaki, L. Treu, P. Tsapekos, G. Luo, S. Campanaro, H. Wenzel, P.G. Kougias, Biogas upgrading and utilization: current status and perspectives, Biotechnol. Adv. 36 (2018) 452–466, https://doi.org/10.1016/j.biotechadv.2018.01.011.

[15] J.A. Mason, T.M. McDonald, T.H. Bae, J.E. Bachman, K. Sumida, J.J. Dutton, S.S. Kaye, J.R. Long, Application of a high-throughput analyzer in evaluating solid adsorbents for post-combustion carbon capture via multicomponent adsorption of CO_2, N_2, and H_2O, J. Am. Chem. Soc. 137 (2015) 4787–4803, https://doi.org/10.1021/jacs.5b00838.

[16] L. Joos, J.A. Swisher, B. Smit, Molecular simulation study of the competitive adsorption of H_2O and CO_2 in zeolite 13X, Langmuir 29 (2013) 15936–15942, https://doi.org/10.1021/la403824g.

[17] K. Hoyer, C. Hulteberg, M. Svensson, J. Jernberg, Ø. Nørregård, Biogas Upgrading – Technical Review, Energiforsk, 2016.

[18] G. Maurin, P.L. Llewellyn, R.G. Bell, Adsorption mechanism of carbon dioxide in faujasites: grand canonical Monte Carlo simulations and microcalorimetry measurements, J. Phys. Chem. B 109 (2005) 16084–16091, https://doi.org/10.1021/jp052716s.

[19] D.G. Boer, J. Langerak, B. Bakker, P.P. Pescarmona, Binderless zeolite LTA beads with hierarchical porosity for selective CO_2 adsorption in biogas upgrading, Microporous Mesoporous Mater. 344 (2022) 112208, https://doi.org/10.1016/j.micromeso.2022.112208.

[20] D.G. Boer, Z. Asgar Pour, J. Langerak, B. Bakker, P.P. Pescarmona, Binderless Faujasite beads with hierarchical porosity for selective CO_2 adsorption for biogas upgrading, Molecules 28 (2023) 2198.

[21] D.G. Boer, D. Čiliak, J. Langerak, B. Bakker, P.P. Pescarmona, Binderless SAPO-34 Beads for Selective CO_2 Adsorption, Sustain, Chem. Clim. Action 2 (2023) 100026, https://doi.org/10.1016/j.scca.2023.100026.

[22] L. Tosheva, J. Sterte, ZSM-5 spheres prepared by resin templating, Stud. Surf. Sci. Catal. 142 (2002) 183–190.

[23] L. Tosheva, V. Valtchev, J. Sterte, Silicalite-1 containing microspheres prepared using shape-directing macro-templates, Microporous Mesoporous Mater. 35–36 (2000) 621–629, https://doi.org/10.1016/S1387-1811(99)00256-5.

[24] L. Tosheva, B. Mihailova, V. Valtchev, J. Sterte, Zeolite beta spheres, Microporous Mesoporous Mater. 48 (2001) 31–37, https://doi.org/10.1016/S1387-1811(01)00327-4.

[25] K. Lin, L. Li, B.F. Sels, P.A. Jacobs, P.P. Pescarmona, Titanosilicate beads as versatile catalysts for the conversion of trioses to lactates and for the epoxidation of alkenes, Catal. Today 173 (2011) 89–94, https://doi.org/10.1016/j.cattod.2011.03.055.

[26] W. Cheng, Y. Jiang, X. Xu, Y. Wang, K. Lin, P.P. Pescarmona, Easily recoverable titanosilicate zeolite beads with hierarchical porosity: preparation and application as oxidation catalysts, J. Catal. 333 (2016) 139–148, https://doi.org/10.1016/j.jcat.2015.09.017.

[27] Z. Asgar Pour, D.G. Boer, S. Fang, Z. Tang, P.P. Pescarmona, Bimetallic zeolite beta beads with hierarchical porosity as Brønsted-Lewis solid acid catalysts for the synthesis of methyl lactate, Catalysts 11 (2021) 1–15, https://doi.org/10.3390/catal11111346.

[28] Z. Asgar Pour, R. Koelewijn, M. El Hariri El Nokab, P.C.A. Van der Wel, K.O. Sebakhy, P.P. Pescarmona, Binder-free zeolite Beta beads with hierarchical porosity: synthesis and application as heterogeneous catalysts for anisole acylation, ChemCatChem (2022) 1–16, https://doi.org/10.1002/cctc.202200518.

[29] A. Ghorbanpour, A. Gumidyala, L.C. Grabow, S.P. Crossley, J.D. Rimer, Epitaxial Growth of ZSM-5 @ Silicalite-1 : A Core-Shell Zeolite Designed with Passivated Surface Acidity, 2015, pp. 4006–4016.

[30] X. Jia, Y. Jeong, H. Baik, J. Choi, A.C.K. Yip, Increasing resolution of selectivity in alkene hydrogenation via diffusion length in core-shell MFI zeolite, Catal. Today 314 (2018) 94–100, https://doi.org/10.1016/j.cattod.2018.02.014.

[31] K. Miyake, Y. Hirota, K. Ono, Y. Uchida, S. Tanaka, N. Nishiyama, Direct and selective conversion of methanol to para-xylene over Zn ion doped ZSM-5/silicalite-1 core-shell zeolite catalyst, J. Catal. 342 (2016) 63–66, https://doi.org/10.1016/j.jcat.2016.07.008.

[32] C. Peng, Z. Liu, Y. Yonezawa, Y. Yanaba, N. Katada, I. Murayama, S. Segoshi, T. Okubo, T. Wakihara, Ultrafast post-synthesis treatment to prepare ZSM-5@Silicalite-1 as a core-shell structured zeolite catalyst, Microporous Mesoporous Mater. 277 (2019) 197–202, https://doi.org/10.1016/j.micromeso.2018.10.036.

[33] M. Okamoto, Y. Osafune, MFI-type zeolite with a core-shell structure with minimal defects synthesized by crystal overgrowth of aluminum-free MFI-type zeolite on aluminum-containing zeolite and its catalytic performance, Microporous Mesoporous Mater. 143 (2011) 413–418, https://doi.org/10.1016/j.micromeso.2011.03.032.

[34] M. Miyamoto, S. Ono, K. Kusukami, Y. Oumi, S. Uemiya, High water tolerance of a core–shell-structured zeolite for CO_2 adsorptive separation under wet conditions, ChemSusChem 11 (2018) 1756–1760, https://doi.org/10.1002/cssc.201800063.

[35] Y. Bouizi, G. Majano, S. Mintova, V. Valtchev, Beads comprising a hierarchical porous core and a microporous shell, J. Phys. Chem. C 111 (2007) 4535–4542, https://doi.org/10.1021/jp068240+.

[36] B. Yan, S. Yu, C. Zeng, L. Yu, C. Wang, L. Zhang, Binderless zeolite NaX microspheres with enhanced CO_2 adsorption selectivity, Microporous Mesoporous Mater. 278 (2019) 267–274, https://doi.org/10.1016/j.micromeso.2018.12.002.

[37] R.J. Argauer, G.R. Landolt, Crystalline Zeolite ZSM-5 and Method of Preparing the Same, US3702886A, 1972. https://patents.google.com/patent/US3702886A/en%0Ahttps://patentimages.storage.googleapis.com/1f/b9/43/ff5945c7fbd9eb/US3702886.pdf.

[38] Y. Wang, T. Du, H. Jia, Z. Qiu, Y. Song, Effect of extra-framework cation in ion-exchanged ZSM-5 from rice husk ash on CO_2 adsorption, Solid State Sci. 97 (2019) 105985, https://doi.org/10.1016/j.solidstatesciences.2019.105985.

[39] J.C. Groen, J. Pérez-Ramírez, Critical appraisal of mesopore characterization by adsorption analysis, Appl. Catal. Gen. 268 (2004) 121–125, https://doi.org/10.1016/j.apcata.2004.03.031.

[40] J.C. Groen, L.A.A. Peffer, J. Pérez-Ramírez, Pore size determination in modified micro- and mesoporous materials. Pitfalls and limitations in gas adsorption data analysis, Microporous Mesoporous Mater. 60 (2003) 1–17, https://doi.org/10.1016/S1387-1811(03)00339-1.

[41] H. Chen, Y.J. Zhang, P.Y. He, C.J. Li, Synthesis, characterization and modification of monolithic ZSM-5 from geopolymer for CO_2 capture: experiments and DFT calculations, Energy 179 (2019) 422–430, https://doi.org/10.1016/j.energy.2019.04.113.

[42] R.S. Pillai, M. Jorge, J.R.B. Gomes, Interaction of atmospheric gases with ETS-10: a DFT study, Microporous Mesoporous Mater. 190 (2014) 38–45, https://doi.org/10.1016/j.micromeso.2014.01.022.

[43] E.P. Hessou, H. Jabraoui, M.T.A.K. Hounguè, J.B. Mensah, M. Pastore, M. Badawi, A first principle evaluation of the adsorption mechanism and stability of volatile organic compounds into NaY zeolite, Zeitschrift Fur Krist. - Cryst. Mater. 234 (2019) 469–482, https://doi.org/10.1515/zkri-2019-0003.